

Received March 10, 2021, accepted March 21, 2021, date of publication March 24, 2021, date of current version March 30, 2021.

Digital Object Identifier 10.1109/ACCESS.2021.3068472

Magnetic Field Energy Harvesting From Current-Carrying Structures: Electromagnetic-Circuit Coupled Model, Validation and Application

YANG KUANG^{ID}, ZHENG JUN CHEW^{ID}, (Member, IEEE), TINGWEN RUAN, AND MEILING ZHU^{ID}

College of Engineering, Mathematics and Physical Sciences, University of Exeter, Exeter EX4 4QF, U.K.

Corresponding author: Meiling Zhu (m.zhu@exeter.ac.uk)

This work was supported in part by the Engineering and Physical Science Research Council (EPSRC), U.K. through the Zero Power, Large Area Rail Track Monitoring under Grant EP/S024840/1, and in part by the Royal Society U.K. through the Industry Fellowship High Performance Energy Harvesting Sensor Systems for Critical Asset Monitoring under Grant INF/R2/202021.

ABSTRACT Magnetic field energy harvesters (MFEHs) from current-carrying structures/conductors are usually modelled as decoupled electromagnetic and electrical systems. The current-carrying structures may affect the performance of MFEH through the generation of the eddy current and the alteration of the magnetic reluctance. Moreover, the load circuit affects the current generated in the coil and therefore the flux density and eddy current generated. The effects of the current-carrying structure and the load circuit cannot be fully described by the decoupled models. This work develops a finite element model (FEM) that fully couples the electromagnetic and electrical systems by simulating both the magnetic field and eddy current distribution of an MFEH connected to an electrical circuit. The FEM first simulates the coil inductance and resistance of a magnetic field energy harvester (MFEH) placed close to a current-carrying structure exemplified by a rail track. The FEM then simulates the outputs of the MFEH connected to an electrical circuit consisting of a compensating capacitor and optimal load resistor determined by the first step. An MFEH was fabricated and tested under a section of current-carrying rail track. Both experiment and simulation show an increase of both coil resistance and inductance when the MFEH is placed close to the rail track. The good agreement between experimental and simulation results validates that the FEM can predict the full-matrix performances of the MFEH, including the coil parameters, power output and magnetic flux density under the influence of the current-carrying structure and the load circuit. Simulation results reveal that in addition to the permeability of the magnetic core, the electrical conductivity and magnetic permeability of the current-carrying structure considerably affect the performance of the MFEH, which cannot be predicted by decoupled models.

INDEX TERMS Magnetic field energy harvesting, finite element model, eddy current loss, rail track energy harvesting.

I. INTRODUCTION

Condition monitoring of critical assets (e.g. overhead power lines and railway) is crucial to enhance the management and maintenance for increased capacity and efficiency. This usually involves a great number of sensors distributed in a large geographic area to monitor and report the status of the assets [1]. Conventional wired sensors require high installation and cabling cost, making them uneconomical for large geographic area deployment. As a result, wireless sensors and sensor networks have attracted significant research

interests and have been playing an increasingly important role in condition monitoring [2]. Traditionally, wireless sensors are powered by batteries, which have a limited energy capacity and lifetime. Once depleted, these batteries need replacement or recharging. The replacement or recharging of batteries can be difficult when the wireless sensors are in great number and/or distributed in a large geographic area. An alternative power source to batteries is energy harvesting (EH), which converts ambient energy to useful electricity to supply wireless sensors [3].

Various location-dependent energy sources are available for energy harvesting, such as solar [4], wind [5], vibration [6], [7] and thermal [8]. Each has its own merits and

The associate editor coordinating the review of this manuscript and approving it for publication was Xiaodong Liang^{ID}.

limitation and has attracted significant research efforts in the past two decades [9]. For assets carrying a high current, a reliable energy source is magnetic fields. Examples of such assets include power transmission lines [10], rail track carrying traction returning current [11] and certain structural beams in aircraft [12]. The magnetic field energy can be scavenged by a piezoelectric cantilever with a tip mass made of permanent magnets [13] or by a magnetoelectric composite through magneto-mechano-electric mechanism [14]. The former method uses the magnetic field to induce elastic strains in the piezoelectric materials through the motion of the permanent magnet, whereas the later through magnetostrictive materials. While these methods convert magnetic field energy indirectly to electricity, a direct and more common method would be the use of magnetic field energy harvesters (MFEHs) based on Faraday's law.

Generally, there are two types of MFEHs: cable-clamped and free-standing [15]. Cable-mounted EHs are wrapped around the magnetic field source—the current conductor [16], [17]. The most common design is a toroid coil with a magnetic core. Maharjan *et al.* [18] used a toroid coil to scavenge electricity from indoor power lines with a current of 65.3 A, which produced 105.24 mW. White *et al.* [19] developed a rectangular coil with flux guides wrapping around a 100 Arms power line, producing average power of 1.5 W. Because the magnetic circuit of cable-mounted EHs is closed and fully encloses the current conductor, they have little demagnetization effect and therefore a high effective permeability. Besides, the magnetic field can be confined within the closed magnetic circuit, leading to little leakage inductance and losses [20]. As a result, cable-mounted EHs can produce high power outputs. However, enclosing the current conductor limits the size and weight of the EH as the EH increases the transmission line sag [21]. Moreover, its application is limited to power transmission lines. When the current conductor is a structural element, e.g. rail track, instead of a cable, enclosing the conductor is not permitted.

Unlike cable-mounted EHs, free-standing EHs have an open magnetic circuit and does not enclose the current conductor. As such, they have greater flexibility and can be applied to broader scenarios. Roscoe and Judd [15] developed a 0.5 m long solenoid with a diameter of 5 cm to collect the magnetic field energy in a substation, which generated 0.3 mW ($0.82 \mu\text{W}/\text{cm}^3$) with an external flux density of $18 \mu\text{T}$. Because the magnetic core of free-standing EHs is open, it has a relatively low effective permeability due to the demagnetization effect [21], leading to relatively low power output. To increase the power output, flux concentrators have been designed as the magnetic core to improve the effective permeability [22], [23]. Yuan *et al.* developed a bow-tie core [21] and a helical core [24] made of MnZn ferrite. When placed in a magnetic field with a flux density of $7 \mu\text{T}_{\text{rms}}$, the bow-tie EH produced $1.86 \mu\text{W}/\text{cm}^3$, which was 2.5 times greater than a conventional solenoid. A higher power density of $2.1 \mu\text{W}/\text{cm}^3$ was achieved by the helical core. While all these magnetic EHs concerned magnetic fields

generated by power lines, Wright *et al.* [12] developed an EH with a funnel-like core to generate electricity from an H-shape current-carrying structural rail used in aircraft. The EH was not tested around the H-shape structure but cables carrying 20 A current. A power output ~ 1 mW was produced when the frequency of the current was 800 Hz.

For the MFEHs mentioned above, finite element and/or analytical models have been used to guide the design. The majority of the models [12], [15], [21], [22], [24] simplified the MFEH as two decoupled systems: one is electromagnetic, which models the conversion of the primary magnetic field generated by the current conductor to an electromotive force (EMF); the other is electrical, which computes the current and power generated by the EMF on an electrical load. The only link between the two decoupled systems is the EMF. However, in reality, the link between electromagnetic and electrical systems can be more complicated. When the EMF generates a current in the coil of the EH, the coil current produces a secondary magnetic field. The secondary magnetic field is superimposed to the primary magnetic field and therefore affects the total flux density in the MFEH, potentially leading to magnetic saturation [20]. A few coupled analytical models were developed to address the magnetic saturation in toroidal coil EHs [20], [25]. However, these models may not fully describe the behaviours of free-standing EHs with an open magnetic circuit. In a free-standing EH, the magnetic field in the EH propagates to the ambient. If the EH is placed in the proximity of the current conductor, which is desirable because the flux density decreases with distance to the conductor, the secondary magnetic field produces circular eddy currents on the current conductor. The generation of the eddy current in return affects the coil inductance and resistance [26], and more importantly the power generation. Moreover, when the current conductor is ferromagnetic, it affects the magnetic path and reluctance [27] of the MFEH placed close and therefore the energy harvesting performance. Both effects cannot be described by the analytical or finite element models mentioned above.

This work, for the first time, develops an electromagnetic-circuit-coupled finite element model for magnetic field energy harvesting from a current-carrying structure, which is exemplified by a rail track. The developed model fully considers the complex coupling between electromagnetic and electrical systems. It can predict the effects of the current-carrying structure on the coil parameters and power output. Moreover, it can directly simulate the full performance matrix of the MFEH connected with a circuit, including the coil parameters, power output and magnetic flux density. Although the model is developed and validated on a solenoid energy harvester, it can be used for the design and optimisation of any MFEHs.

II. THEORETICAL ANALYSIS

This study concerns energy harvesting from the magnetic field generated by current-carrying structures. One example of such structures is a rail track, which is usually used as

the returning path of traction current in an electrified railway [28]. When the traction current is AC, which is the case in the UK [29], the varying magnetic field can be converted to electricity. The simplest energy harvester perhaps is a solenoid placed close to the rail track, as shown in Fig. 1. When a harmonic current with a zero-peak amplitude of I_s and frequency of ω is running in the track, the resulted varying magnetic field produces an EMF in the coil, which is [21]

$$V_{oc} = N\omega A_e \mu_e B_{ex} = N\omega A_e B_{oc} \quad (1)$$

where N is the total number of windings in the coil; A_e and μ_e are the effective cross-section area and effective relative permeability of the magnetic core; B_{ex} is the external flux density generated by the track; $B_{oc} = \mu_e B_{ex}$ is the flux density in the magnetic core when the coil is open-circuited.

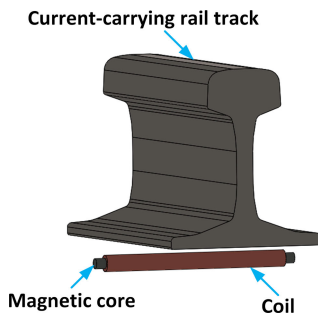


FIGURE 1. A schematic of solenoid energy harvester in the vicinity of a current-carrying rail track.

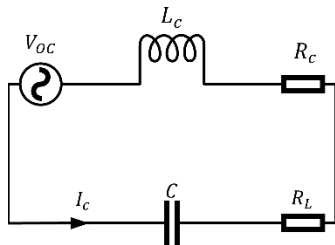


FIGURE 2. An equivalent circuit model for the solenoid energy harvester.

When used for energy harvesting, the solenoid can be represented by an equivalent circuit model [21] shown in Fig. 2. R_c and L_c are the resistance and inductance of the coil, respectively. R_L is the load resistance and C is a compensating capacitor used to tune out the impedance of the coil inductance. The value of C therefore is

$$C = \frac{1}{\omega^2 L_c}. \quad (2)$$

When the coil resistance is known and $R_L = R_c$, the average power output reaches the maximum:

$$P = \frac{V_{oc}^2}{8R_c} = \frac{(N\omega A_e \mu_e B_{ex})^2}{8R_c}. \quad (3)$$

The power output is proportional to B_{ex}^2 . Because the flux density generated by a current conductor decreases rapidly

with the distance away to the conductor, it is desirable to place the solenoid close to the conductor to produce higher power.

The coil resistance and inductance cannot be accurately determined without considering the coupling between the electromagnetic system (represented by (2-3)). When a current I_c is generated in the coil by the EMF, the current produces a varying magnetic field. The flux density in the middle of the solenoid is [27]

$$B_s = \frac{\mu_e N I_c}{l_c} \quad (4)$$

where l_c is the length of the coil. B_s is superimposed to the primary magnetic field B_{oc} , forming the total flux density B in the solenoid. Because I_c is dependent on the load resistance, both B_s and B also depends on the load resistance.

The magnetic field generated by the solenoid produces circular eddy currents in the magnetic core if the core material is electrically conductive, leading to an increase of coil resistance. When materials with low conductivity such as MnZn ferrite are used for the magnetic core, the eddy current loss in the core can be ignored. However, as the magnetic path of a solenoid is open, the magnetic field propagates to space outside the magnetic core, producing circular eddy currents on the surface of the current-carrying structure if the solenoid is placed close to the structure. The energy loss leads to the increase of the coil resistance, which can be expressed as

$$R_c = R_w + R_{ed} = R_w + \frac{2P_{ed}}{I_c^2} \quad (5)$$

where R_w is the wire resistance of the coil; $R_{ed} = 2P_{ed}/I_c^2$ is the coil resistance resulted from the eddy current; P_{ed} is the power dissipation of the eddy current. In a decoupled model, the R_{ed} is ignored and the coil resistance only considers the wire resistance.

In addition to increasing the coil resistance, the eddy currents on the structure generate a magnetic field opposing the one in the solenoid [26]. Moreover, the rail track is made of ferromagnetic material. It alters the magnetic path of the solenoid and reduces magnetic reluctance [30]. Both the eddy current and the variation of the magnetic reluctance affects the magnetic flux through the coil and therefore affect the coil inductance since the coil inductance is [31]

$$L_c = \frac{N\varnothing_m}{I_c} = \frac{\mu_e \mu_0 N^2 A_e}{l_c} \quad (6)$$

where \varnothing_m is the average magnetic flux through each winding of the coil. Furthermore, (6) further suggests that the variation of the coil inductance means the alteration of the effective permeability μ_e , which will results in the variation of the EMF according to (1).

From the analysis above, it can be seen that the coil inductance, resistance and open-circuit voltage are affected by the current-carrying structure. The accurate modelling requires the full coupling between the electromagnetic and electrical systems. Analytical modelling of the EH in Fig. 1 is difficult because of the complex shape of the current-carrying

structure. Therefore, this work develops an electromagnetic-circuit-coupled finite element model to predict the performance of the EH.

III. FINITE ELEMENT MODELLING METHODS

The finite element model was developed in COMSOL Multiphysics®. The 3D geometry built for the FEM is shown in Fig. 3. An air cylinder (diameter: 750 mm; height:500 mm) was built to enclose the rail track and the solenoid energy harvester. Unless specified, the geometrical parameters and material properties used for the FEM are listed in Table 1.

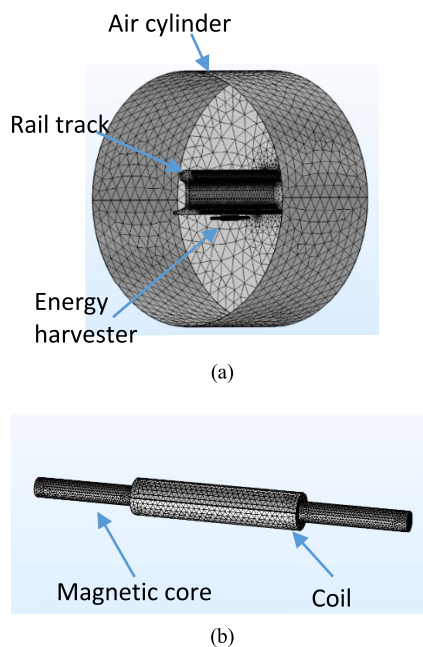


FIGURE 3. The meshed geometry of the finite element model (a) the full model (b) a close-up view of the meshed solenoid energy harvester.

The magnetic core and the rail track were defined as ferromagnetic material. The magnetization of a ferromagnetic material depends nonlinearly on the magnetic field strength due to the magnetic hysteresis, leading to variable magnetic permeability. Including the nonlinear magnetization and magnetic hysteresis in the FEM is challenging for frequency domain analysis. In this study, a linear magnetization model of the ferromagnetic material was used by defining a constant magnetic permeability for the ferromagnetic materials. The linear magnetization model is valid when the magnetic field and the hysteresis loss is relative low, which is the case of this study and has been widely used in the modelling of magnetic field energy harvesters [12], [15], [21], [22], [24]. When the magnetic core is saturated or the hysteresis loss is significant, the linear magnetization model may not be valid and the FEM may overestimate the power output considerably. Moreover, it must be noted that the magnetic permeability of ferromagnetic materials usually decreases as the temperature increases. The material properties at room temperature were used in this study. MnZn Ferrite was assumed to be the

TABLE 1. Geometrical parameters and material properties used in the simulation.

Symbol	Description	Value	Unit
d	Diameter of the magnetic rod	10	mm
l	Length of the magnetic rod	200	mm
l_c	Length of the coil	180	mm
N	Number of coil windings	27000	
d_w	Diameter of coil wire	0.2	mm
d_i	Internal diameter of coil	10	mm
d_o	Outer diameter of coil	22	mm
l_t	Length of the rail track	500	mm
d_c	Distance between EH and track	20	mm
μ_s	Relative permeability of current-carrying structure	20	
σ_r	Electrical conductivity of the current-carrying structure	3×10^6	S/m
μ_c	Relative permeability of the magnetic core	2000	
σ_c	Electrical conductivity of the magnetic core	1	S/m
I_s	Current running through the structure in Power-output Study	100	A
I_{c0}	Current input in the coil in Coil-parameter Study	0.01	A

material of the magnetic core, which has a very small electrical conductivity and therefore hardly results in eddy current loss in itself.

The coil was modelled as a hollow cylinder, as shown in Fig. 3 (b), with an internal diameter of d_i and an outer diameter of d_o . The coil was defined as a circular type of coil in COMSOL. The number of windings N , the diameter d_w and the electrical conductivity of the coil wire were assigned. The average perimeter of the coil windings is calculate by

$$\bar{l}_w = \pi \cdot \frac{d_i + d_o}{2} \tag{7}$$

This value was assigned to be the ‘length of the edges’ in the coil model of COMSOL. The coil wire length in COMSOL is calculated by timing ‘length of the edges’ with the number of windings. The FEM then computes the wire resistance based on the coil wire length, diameter and electrical conductivity. Therefore, the accuracy of ‘length of the edges’ is very important for the accurate simulation of coil resistance.

The FEM consists of two studies: Coil-parameter Study to simulate the coil inductance and resistance, and Power-output Study to simulate the power generation and total flux density. Both studies were harmonic analysis performed at 50 Hz. Magnetic insulation was assigned to the exterior surfaces of the air cylinder. A boundary condition ‘Gauge Fixing for A-Field’ was added to speed up the convergence and reduce the computational time [32].

In the Coil-parameter Study, the structure was not energised but the coil was excited with a current I_{c0} by setting the ‘coil excitation’ as ‘current’. The coil current produces a voltage V_{c0} across the coil, as shown in Fig. 4. The ratio of V_{c0} and I_{c0} , which is the complex impedance of the coil, was used

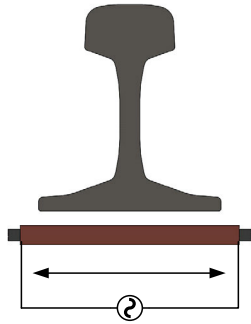


FIGURE 4. Boundary conditions of the coil-parameter study.

to identify the coil inductance L_c and resistance R_c . The entire model was built in the ‘Magnetic and Electrical Interface’ (MEI) of COMSOL. MEI can compute the magnetic field and eddy current distribution by applying Ampere’s Law and Current Conservation [32]. As such, the L_c and R_c simulated in this study took into account the effect of the eddy current and the ferromagnetic rail track, whereas the traditional decoupled models assumed a large distance between the conductor and the MFEH, and only considered the wire resistance for the coil resistance [12], [15], [21], [22], [24].

In the Power-output Study, the cross-sections at both ends of the structure were used as electrodes and a current I_s was input through the two electrodes, as shown in Fig. 5 (a). The rail track and the MFEH were modelled in the MEI. Therefore, the coil parameters and voltage output of the coil in this study included the effects of the eddy current and the ferromagnetic rail track. Unlike traditional decoupled modelling [12], [21], [22], [24], where the MFEH is open-circuited and only the open-circuit voltage can be simulated, the coil output in the present model was connected to an ‘Electric Circuit Interface’ (ECI), which consisted of a compensating capacitor C and a load resistance R_L (Fig. 5 (b)). The value of C was computed based on L_c simulated in Coil-parameter Study and according to (2). The value of R_L , unless specified, was set to R_c simulated in Coil-parameter Study to obtain the maximum power output. The current I_c and magnetic field B_s generated by the coil depended on the voltage output simulated by the MEI and the circuit simulated in the ECI. The eddy current loss generated in the MEI also depended on B_s and therefore the circuit as well. In this way, the electromagnetic and electrical (circuit) domains of the MFEH are coupled together.

The model can take advantage of the symmetry of the geometries to build half of the model, leading to reduced computation time. In this work, a full model was used to present the current and magnetic flux distribution more clearly.

IV. EXPERIMENTAL METHODS

To validate the FEM, a solenoid energy harvester was fabricated, as shown in Fig. 6. The magnetic core is made of MnZn Ferrite 3B1 with a diameter of 10 mm and a length of 200 mm. MnZn Ferrite 3B1 has an initial relative permeability of 900,

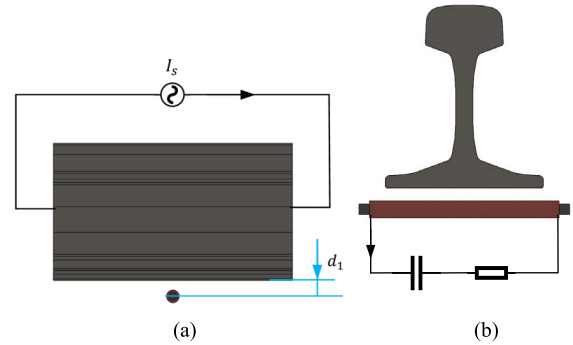


FIGURE 5. Boundary conditions of the power-output study: (a) the rail track is energized with I_s ; (b) the solenoid energy harvester is connected to a circuit consisting of a compensating capacitor and a load resistor.



FIGURE 6. The fabricated solenoid energy harvester.

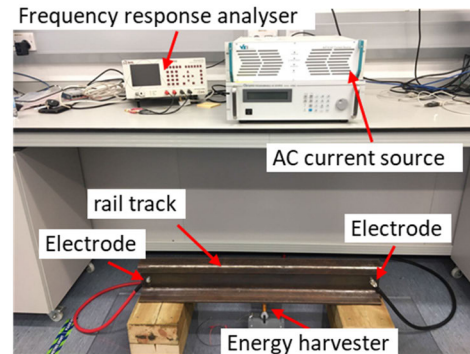


FIGURE 7. Experimental setup.

a saturation limit of 0.38 T and electrical conductivity of 0.2 S/m. The coil was wound in the lab by a coil winding machine (CNC200 A). It features $\varnothing 0.2$ mm copper wire, coil length l_c of 88.9 mm and outer diameter d_o of 18.8 mm. It has in total 17 layers and 6086 turns of winding.

The solenoid energy harvester was placed underneath a rail track, as shown in Fig. 7. The 50 Hz AC running in the rail track was provided through two bolted electrodes by an AC source (A5710-400-2V0, VX Instruments GmbH). The current supplied by the AC source was monitored by a current probe (Pico Technology TA167).

When measuring the coil resistance and inductance, the rail track was not energised and the solenoid was connected to a frequency response analyser (PSM1700, Newton 4th). The frequency response analyser energised the solenoid at 50 Hz with a voltage of 1 V and computed the coil inductance and resistance according to the measured voltage and current in the coil. Before measuring the power output, multi-layer ceramic capacitors (tolerance $\pm 20\%$) were connected in series to the coil to tune out the coil inductance. The value

of the capacitance was adjusted through a combination of a few capacitors until the total impedance of the coil and the capacitors, measured by the frequency response analyser at 50 Hz, had negligible reactive part. Following that, a variable load resistance was connected to the capacitor and the coil. The rail track was then energised with the current waveform and amplitude monitored by the current probe. The voltage across the load resistor was measured to calculate the average power output.

V. RESULTS AND DISCUSSIONS

A. EXPERIMENTAL VALIDATION OF COIL-PARAMETER STUDY

To compare the simulation results with the experiment, the coil parameters in the FEM were selected to match the experiment: $l_c = 9$ mm, $d_o = 18.8$ mm and $N = 6086$. The simulated coil resistance and inductance are compared with the experimental results in Table 2. d_1 is the distance between the solenoid and the rail track, as denoted in Fig. 5(a). The simulation results are in good agreement with the experiment. $d_c = \infty$ means the coil parameters were measured or simulated without the presence of the rail track. When $d_1 = 77$ mm, the coil resistance and inductance are about the same as $d_1 = \infty$, suggesting the negligible effect of the rail track at this distance. As the solenoid is moved closer to the track, both coil resistance and inductance increase. When $d_1 = 15$ mm, the coil resistance is increased by 38%, compared to $d_1 = \infty$.

TABLE 2. Comparison of measured and simulated coil resistance and inductance.

d_1 (mm)	Coil resistance R_c (Ω)		Coil inductance L_c (H)	
	Experiment	FEM	Experiment	FEM
∞	155.2	153.5	3.93	3.93
77	155.8	157.5	3.94	3.97
43	164.2	166.8	4.01	4.08
15	214.2	218.7	4.59	4.67

The increase of the coil resistance is due to the additional energy loss resulted from the induced eddy current on the rail track. This can be evidenced by the induced eddy current on the rail track during the Coil-parameter Study, as shown in Fig. 8. Although the rail track is not energised, current density up to 2.5×10^4 A/m is observed, which is induced by the magnetic field generated by the energised coil. The eddy current generates a magnetic field, which opposes the field generated by the coil current and tends to reduce the total magnetic flux through the coil, leading to a reduced coil inductance by (6). However, the ferromagnetic track alters the path of the magnetic flux outside the coil and reduces the magnetic reluctance of the MFEH, similar to the mechanism used in variable reluctance energy harvesting [30]. This leads to an increase of the magnetic flux through the coil and tends

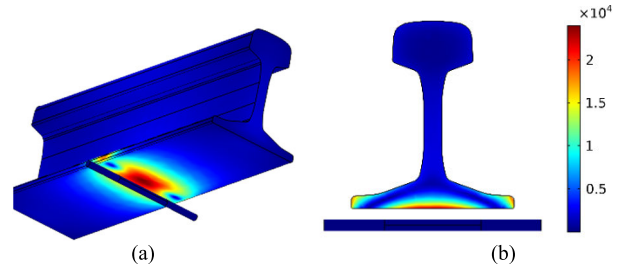


FIGURE 8. Eddy current density generated on the rail track by the solenoid placed at $d_1 = 15$ mm when the coil is energized with $I_{c0} = 0.01$ A and the rail track is not energized: (a) perspective view and (b) cross-section view. Unit: A/m².

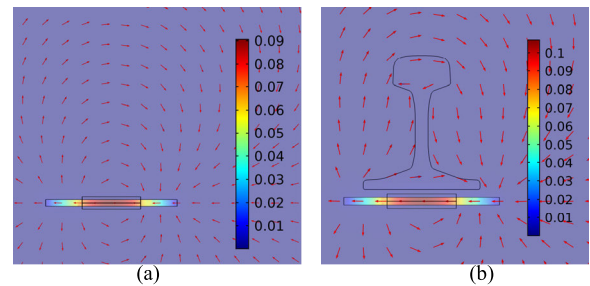


FIGURE 9. Magnetic flux density when the coil is placed at $d_1 = 15$ mm and energized with $I_{c0} = 0.01$ A: (a) the rail track is not present; (b) the rail track is present but not energized. Unit: T.

to increase the coil inductance. The increase of the magnetic flux because of the ferromagnetic rail overshadows the reduction of the magnetic flux due to the eddy current. As a result, the total magnetic field through the coil is increased, as shown in Fig. 9. The average flux density in the middle of the magnetic core is denoted as B_1 for the Coil-parameter study in this work. B_1 is increased from 0.09 T to 0.107 T when the rail track is present. Consequently, the coil inductance is increased.

B. EXPERIMENTAL VALIDATION OF POWER-OUTPUT STUDY

The measured open-circuit voltages are compared with simulation in Fig. 10 for $d_c = 15$ and 77 mm. The simulated and measured V_{oc} increases linearly with the current I_s in the track at both positions because the flux density B_{ex} generated by the track increases linearly with I_s , which can be verified by the simulated B_{oc} in the figure. The distribution of B_{oc} in the magnetic core is similar to Fig. 9 (b) and therefore is not repeatedly presented. The values of B_{oc} were taken as the average flux densities in the middle of the magnetic core. The B_{oc} calculated this way was found to accurately represent the average flux density in the coil, which can be validated by the close agreement of V_{oc} simulated by the FEM and calculated by (1). When the solenoid is placed closer to the rail track, a higher flux density and therefore higher V_{oc} is generated. The good agreement between simulation and experiment suggests the accurate modelling of the current and flux distribution in the rail track as well as the effective permeability of the solenoid.

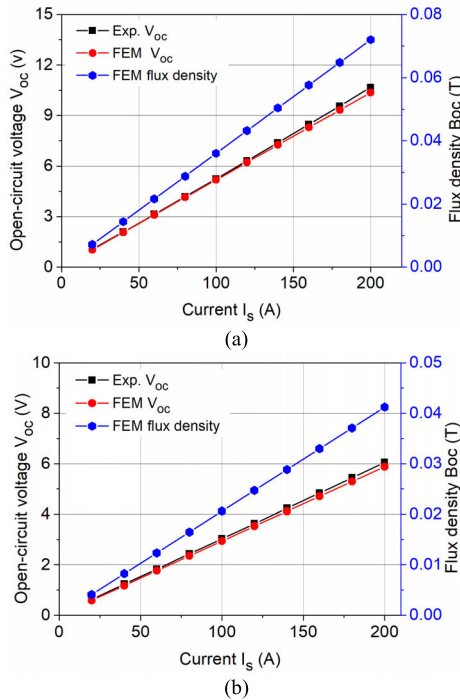


FIGURE 10. Comparison of simulated and measured open-circuit voltages and flux densities of the solenoid energy harvester when (a) $d_1 = 15$ mm (b) $d_1 = 77$ mm.

The measured power, voltage and current outputs are compared with simulation in Fig. 11 for $d_1 = 15$. In the simulation, the load resistance was kept constant at the coil resistance. In the experiment, 10 values of R_L ranging from 50 to 1000 Ω were used although only a few values of R_L are presented for the clarity of the figures. The value of the capacitance used in the experiment was 2.17 μ F. The impedance of the coil with the capacitor has a resistive and reactive component of 245.6 and -4.9 Ω , respectively. The increase of the resistance from 214.2 to 245.6 Ω is due to the resistive component of the capacitors.

The measured power agrees well with the simulation when I_s is low. At $I_s = 50$ A, the power measured is 3.5 mW, compared with 3.7 mW in the simulation, as shown in Fig. 12 (a). As I_s is increased, there is a gradual increase in the discrepancy between simulation and experiment. At $I_s = 200$ A, the power measured is 50.5 mW, compared to 61.0 mW in simulation, as shown in Fig. 12 (b), and the optimal load resistance has increased to 400 Ω . The reduction in the power output and the increase in the optimal load resistance compared with simulation are because of the nonlinear magnetization of the core at high flux density [20], [25] and the variation in the properties of the capacitor at high voltage [33]. The total flux density B during energy harvesting is much higher than the open-circuit flux density B_{oc} due to the magnetic field generated by the current in the coil, although the distribution is about the same as Fig. 9 (b). The average value of B in the middle of the magnetic core presented in Fig. 10 and 11.

As the load resistance increases, the flux density in the magnetic core decreases monotonically, as shown in Fig. 12.

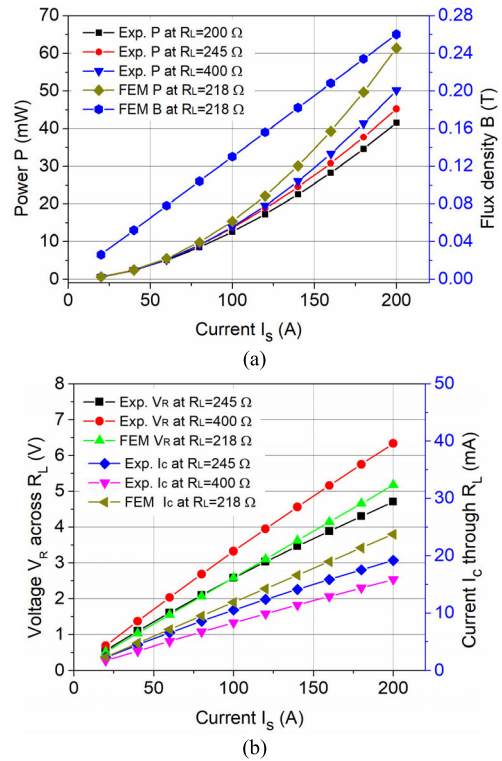


FIGURE 11. (a) The simulated and measured power outputs & the simulated flux density; (b) the simulated and measured voltage and current outputs when of the solenoid energy harvester placed at $d_1 = 15$ mm. The simulated flux density is taken as the average in the middle of the magnetic core.

This means increasing the load resistance can reduce the effects of nonlinear magnetization on L_c by reducing the total flux density. The increase in the load resistance also reduces the voltage on the capacitor and therefore reduces the variation in its properties including the resistance loss and capacitance [33], leading to a better match of L_c and C , which leads to the maximum power output at a higher R_L . Moreover, Fig. 12 shows a slight increase in R_L beyond the optimal resistance does not reduce the power output significantly. This partly attributes to the increase of the optimal load resistance in the experiments.

The measured power, voltage and current outputs are compared with simulation in Fig. 13 for $d_1 = 77$. The load resistance in the simulation was kept constant at 157 Ω whereas 10 different load resistors were used in the experiment, although only the power output of 4 load resistors are presented in the figure for clarity. The compensating capacitor used in the experiment was 2.55 μ F. The impedance of the coil with the capacitor has a resistive and reactive component of 159.4 and -0.9 Ω , respectively. The optimal load resistance in the experiment was found to increase with the current in the rail track, similar to the observations with $d_1 = 15$ mm. When the current I_s in the rail track is less than 50 A, the measured optimal load resistance is 157 Ω , which is about the same as the impedance of the coil and the compensating capacitor. At $I_s = 200$ A, the measured

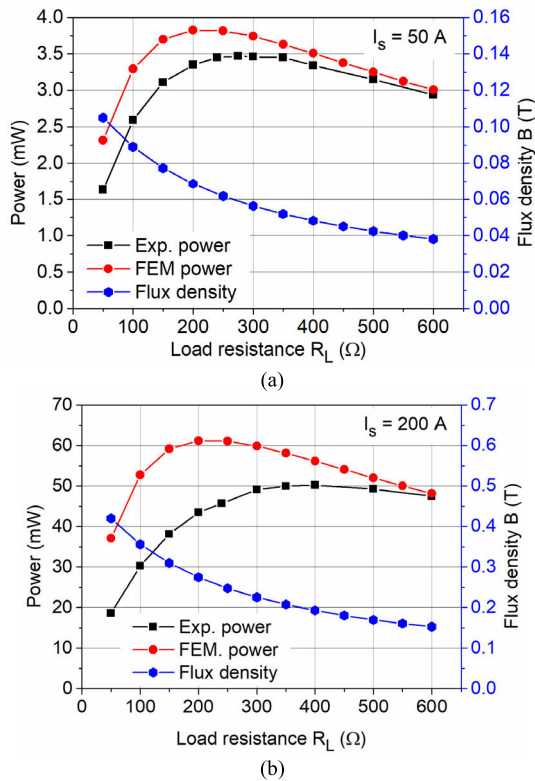


FIGURE 12. Effects of the load resistance on the power output and flux density of the solenoid energy harvester placed at $d_1 = 15$ mm for (a) $I_s = 50$ A and (b) $I_s = 200$ A.

optimal load resistance is increased to 300Ω , producing 24.5 mW of power compared to 27.4 mW in simulation. The discrepancy between the measured and simulated power, in this case, is smaller than $d_1 = 15$ mm. This is likely because the flux density at $d_1 = 77$ mm is lower, leading to a reduced effect of the nonlinear magnetization and hysteresis loss. The measured power at $d_1 = 15$ mm is about twice that at $d_1 = 77$ mm despite the increased eddy current losses. This validates the benefits of placing the MFEH close to the current conductor.

C. THE MATERIAL PROPERTIES OF THE CURRENT-CARRYING STRUCTURE

Although a rail track is used in this study, the current-carrying structure may be made of other materials. Therefore, the effects of the structure’s material properties including the electrical conductivity and magnetic permeability were investigated by the developed model.

As the electrical conductivity σ_s of the current-carrying structure increases, the eddy current density, simulated by the Coil-parameter Study increases, as shown in Fig. 14(a). As a result, the magnetic field produced by the eddy current increases. Because the magnetic field produced by the eddy current opposes the magnetic field produced by the coil current, its increase leads to the reduction of the total magnetic field B_1 through the coil, as shown in Fig. 14(a). Therefore the coil inductance is reduced, agreeing with (6). Although

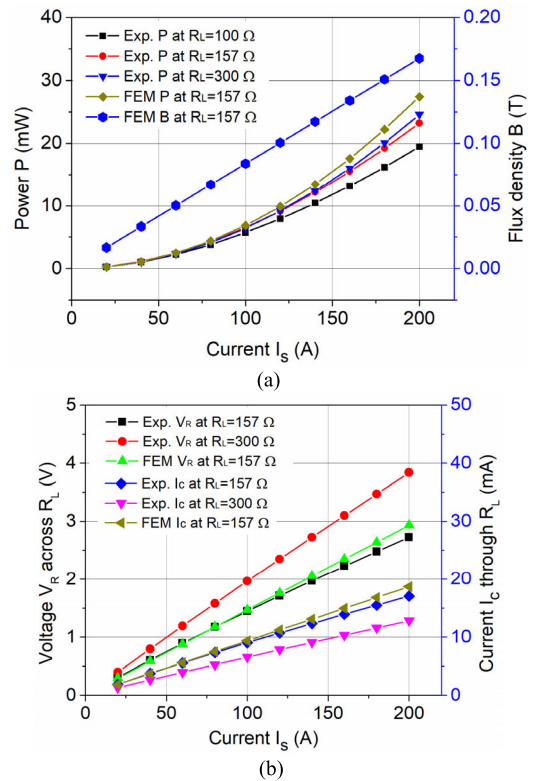


FIGURE 13. (a) The simulated and measured power outputs & the simulated flux density; (b) the simulated and measured voltage and current outputs when of the solenoid energy harvester placed at $d_1 = 77$ mm. The simulated flux density is taken as the average in the middle of the magnetic core.

the eddy current increases monotonously with σ_s , the resulted power loss P_{ed} , predicted by the FEM, first increases and then decreases with σ_s , as shown in Fig. 14 (b). This is because the power loss is not just related to the eddy current amplitude but also depends on the resistance of the loops described by the flow of eddy currents, which is expected to decrease with σ_s . The coil resistance R_c follows the same trend as P_{ed} . This is because R_{ed} , the resistance due to eddy current loss, is proportional to P_{ed} , according to (5). The values of R_{ed} calculated by (5) is presented in Fig. 14(b). The difference between R_c and R_{ed} is always the wire resistance R_w , which is 0.72 k Ω for the present coil.

The effect of σ_s on the open-circuit voltage and power output, simulated by the Power-output Study is shown in Fig. 15. σ_s has limited impact on the open-circuit voltage V_{oc} because the current in the structure is kept constant. The power output first decreases and then slightly increases with σ_s , which is the result of the variation of R_c with σ_s .

As the relative permeability μ_s of the structure increases, the eddy current simulated in the Coil-parameter Study increases, as shown in Fig. 16(a). As a result, the magnetic field produced by the eddy current is expected to increase with μ_s . The flux density B_1 through the coil, which is weakened by the magnetic field of the eddy current, first increases with μ_s and then gradually flattens, suggesting

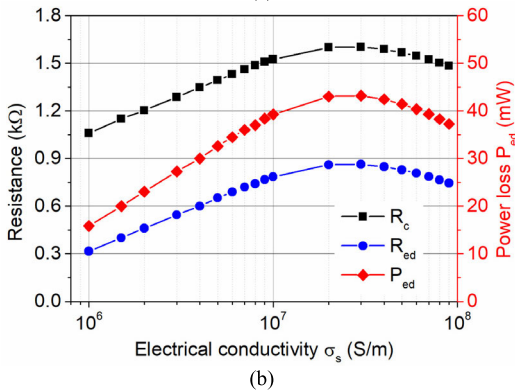
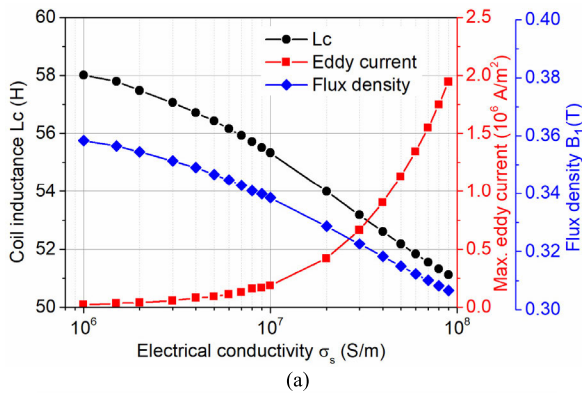


FIGURE 14. Effect of the electrical conductivity σ_s of the current-carrying structure on (a) the coil inductance L_c , maximum eddy current density and the average flux density in the middle of the magnetic core; (b) the coil resistance R_c , the power loss resulted from eddy current and the calculated R_{ed} .

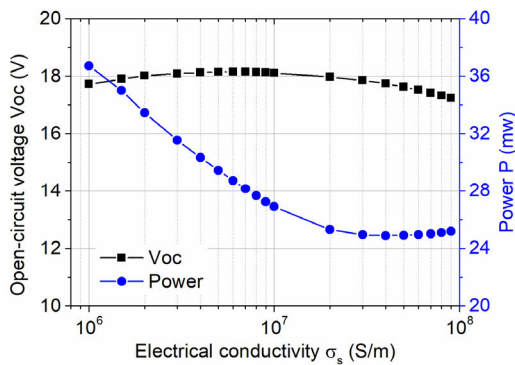


FIGURE 15. Effects of the electrical conductivity σ_s of the current-carrying structure on the open-circuit voltage and power output when the structure carries a current of 100 A.

that the increase of μ_s leads to an increase in the magnetic field generated by the coil current. This is because the ferromagnetic structure alters the magnetic path outside the coil and concentrates the magnetic field generated by the coil current [26]. When $\mu_s < 100$, the increase of the magnetic field generated by the coil current is larger than the increase of the opposing magnetic flux from the eddy current, leading to the increase in B_1 . As μ_s is increased further, the increase of the magnetic field generated by the coil current is about the same as the increase of the opposing magnetic field from

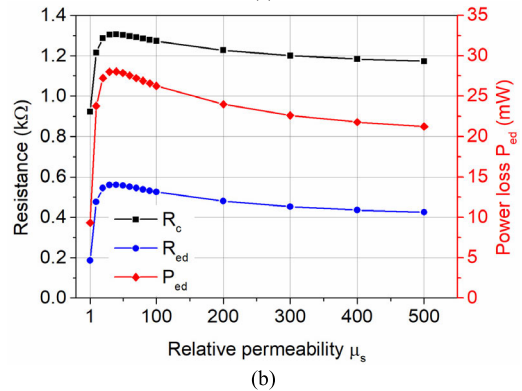
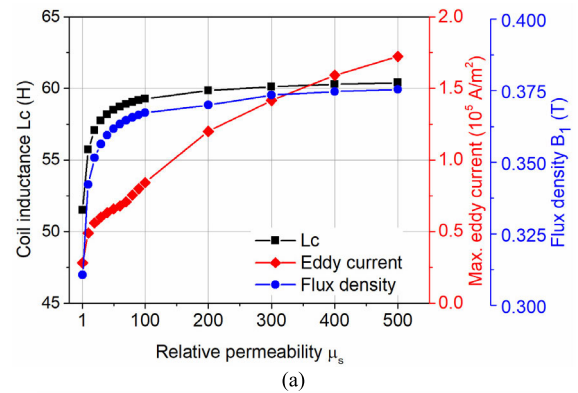


FIGURE 16. Effect of the relative permeability μ_s of the current-carrying structure on (a) the coil inductance L_c , maximum eddy current density and the average flux density in the middle of the magnetic core; (b) the coil resistance R_c , the power loss P_{ed} resulted from eddy current and the calculated R_{ed} .

the eddy current, leading to the gradual flattening of B_1 . This suggests as μ_s is large enough, the structure's capability of increasing the flux density diminishes. This is likely caused by the saturation of its effective permeability, similar to the saturation of the effective permeability of the magnetic core that is discussed in Figure 18.

The coil inductance L_c follows the trend of the flux density B_1 —it increases rapidly with μ_s when $\mu_s < 100$. As μ_s is increased further, its effect on L_c diminishes. The power loss due to eddy current shows a different pattern from the eddy current density shown in Fig. 16(b), as the power loss also depends on the resistance of the loops described by the flow of eddy currents. The coil resistance R_c follows the trend of power loss, as expected. μ_s has minimal effects on the open-circuit voltage as shown in Fig. 17. This is because in the open-circuit condition, the coil current is zero and does not generate a magnetic field interacting with the current-carrying structure. The variation of the power output is mainly caused by the variation of R_c with μ_s .

D. THE PROPERTIES OF THE MAGNETIC CORE

The effects of the relative permeability of the magnetic core were investigated with the conditions listed in Table 1. As shown in Fig. 18, when μ_c increases, all the parameters including the coil resistance, inductance, open-circuit voltage

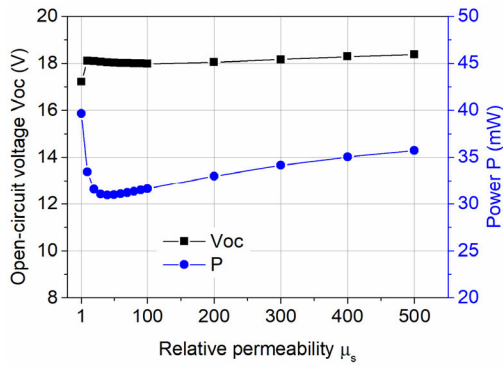


FIGURE 17. Effect of the relative permeability μ_s of the current-carrying structure on the open-circuit voltage and power output when the structure carries a current of 100 A.

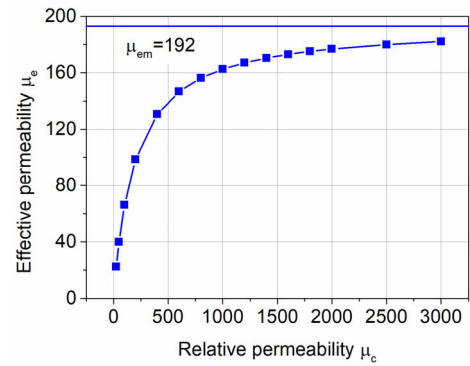


FIGURE 19. Effective permeability of the ferromagnetic rod against the relative permeability.

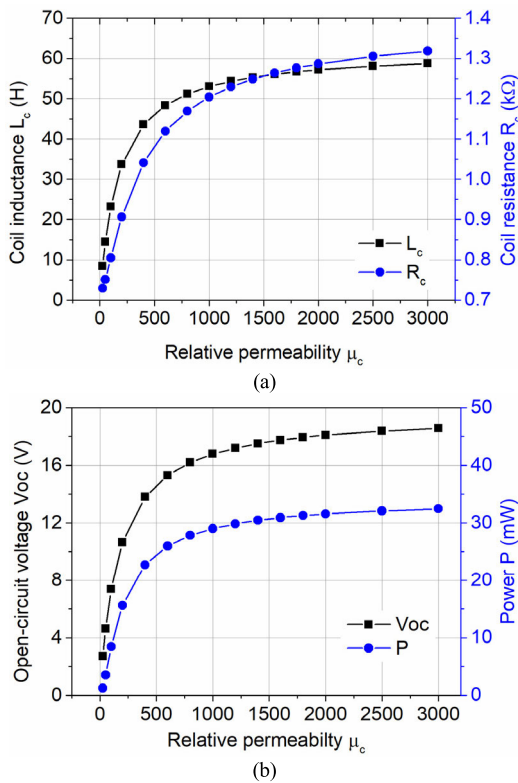


FIGURE 18. Effects of the relative permeability of the magnetic core on (a) coil resistance and inductance simulated in coil-parameter study (b) open-circuit voltage and power output simulated in power-output study.

and power output first increase and then gradually flatten. This trend is caused by the variation of the effective permeability μ_e of the magnetic core. μ_e of a rod can be expressed as [34]

$$\mu_e = \frac{\mu_c}{1 + 0.84 \left(\frac{d}{l}\right)^{1.7} (\mu_c - 1)} \quad (8)$$

where d and l are the diameter and length of the rod, respectively. When d and l are fixed, μ_e first increases with μ_c , as shown in Fig. 19. As μ_c increases further, its effect diminishes and it will finally saturate at a maximum value μ_{em} that

depends only on the dimensions of the rod:

$$\mu_{em} = \lim_{\mu_c \rightarrow \infty} \mu_e = \frac{1}{0.84 \left(\frac{d}{l}\right)^{1.7}} \quad (9)$$

The coil inductance L_c and the open-circuit voltage V_{oc} follows the variation of μ_e as they are proportional to μ_e , according to (6) and (1), respectively. As μ_e increases, the coil produces a stronger magnetic field in the Coil-parameter Study, which produces a higher eddy current and power loss. As a result, the coil resistance R_c is also proportional to μ_e . The variation of V_{oc} and R_c leads to the variation of the power output P against μ_c . The maximum power output can be obtained when $\mu_c = 1000$. Further increase in μ_c hardly increases the power output. Since the coil resistance R_c increases with the effective permeability, it is expected the increase of R_c will be more significant when magnetic cores with higher effective permeability are used around large conductors, such as the funnel core [12] and helical core [24] reported in the literature.

VI. CONCLUSION

In this work, an electromagnetic-circuit-coupled finite element model (FEM) of magnetic field energy harvesters (MFEHs) was developed, validated and applied energy harvester design. The Coil-parameter study of the FEM was developed in the ‘Magnetic and Electric Interface’ (MEI) of COMSOL, which is capable of computing the magnetic field and eddy current distribution. The simulated coil resistance and inductance, therefore, included the effects of the eddy current and the ferromagnetic conductor, opposed to the traditional models which only considered the wire resistance as the coil resistance. The Power-output study of the FEM consisted of the current-carrying rail track and the MFEH modelled in the MEI and an electrical circuit modelled in the ‘Electrical Circuit Interface’. The coil output was connected to the electrical circuit, in contrast to the open-circuit coil in traditional decoupled models. The FEM could simulate the power output and total flux density in the magnetic core under the influence of not just the effects of the eddy current and ferromagnetic conductor, but also the connected circuit. The simulation results were validated by experiment with

good agreement. Further studies were performed by using the developed model to investigate various factors that affected the performance of the MEH.

When the MEH is placed close to the current-carrying structure, its coil resistance and inductance are affected by the structure through the generation of eddy current on the structure and the alternation in the magnetic reluctance of the MFEH. This in return affects the power output. This phenomenon was predicted by the simulation and validated by experiment. The variation of the coil resistance and inductance depends on the electrical conductivity and magnetic permeability of the current-carrying structure. Notably, the power loss due to the eddy current does not increase monotonically with the electrical conductivity of the structure because the power loss is related to both the eddy current amplitude and the resistance of the loops described by the flow of eddy currents. The coil resistance and inductance are found to increase with the effective permeability of the magnetic core due to a higher eddy current generation on the current-carrying structure.

REFERENCES

- [1] P. Fraga-Lamas, T. Fernández-Caramés, and L. Castedo, "Towards the Internet of smart trains: A review on industrial IoT-connected railways," *Sensors*, vol. 17, no. 6, p. 1457, Jun. 2017.
- [2] V. J. Hodge, S. O'Keefe, M. Weeks, and A. Moulds, "Wireless sensor networks for condition monitoring in the railway industry: A survey," *IEEE Trans. Intell. Transp. Syst.*, vol. 16, no. 3, pp. 1088–1106, Jun. 2015.
- [3] R. Calió, U. B. Rongala, D. Camboni, M. Milazzo, C. Stefanini, G. De Petris, and C. M. Oddo, "Piezoelectric energy harvesting solutions," *Sensors*, vol. 14, no. 3, pp. 4755–4790, Mar. 2014.
- [4] X. Tang, X. Wang, R. Cattley, F. Gu, and A. Ball, "Energy harvesting technologies for achieving self-powered wireless sensor networks in machine condition monitoring: A review," *Sensors*, vol. 18, no. 12, p. 4113, Nov. 2018.
- [5] A. B. Rostami and M. Armandei, "Renewable energy harvesting by vortex-induced motions: Review and benchmarking of technologies," *Renew. Sustain. Energy Rev.*, vol. 70, pp. 193–214, Apr. 2017.
- [6] Y. Kuang, Z. J. Chew, and M. Zhu, "Strongly coupled piezoelectric energy harvesters: Finite element modelling and experimental validation," *Energy Convers. Manage.*, vol. 213, Jun. 2020, Art. no. 112855.
- [7] Y. Kuang and M. Zhu, "Parametrically excited nonlinear magnetic rolling pendulum for broadband energy harvesting," *Appl. Phys. Lett.*, vol. 114, no. 20, May 2019, Art. no. 203903.
- [8] Z. Lu, H. Zhang, C. Mao, and C. M. Li, "Silk fabric-based wearable thermoelectric generator for energy harvesting from the human body," *Appl. Energy*, vol. 164, pp. 57–63, Feb. 2016.
- [9] F. K. Shaikh and S. Zeadally, "Energy harvesting in wireless sensor networks: A comprehensive review," *Renew. Sustain. Energy Rev.*, vol. 55, pp. 1041–1054, Mar. 2016.
- [10] W. Wang, X. Huang, L. Tan, J. Guo, and H. Liu, "Optimization design of an inductive energy harvesting device for wireless power supply system overhead high-voltage power lines," *Energies*, vol. 9, no. 4, p. 242, Mar. 2016.
- [11] A. Mariscotti, P. Pozzobon, and M. Vanti, "Distribution of the traction return current in AT electric railway systems," *IEEE Trans. Power Del.*, vol. 20, no. 3, pp. 2119–2128, Jul. 2005.
- [12] S. W. Wright, M. E. Kiziroglou, S. Spasic, N. Radosevic, and E. M. Yeatman, "Inductive energy harvesting from current-carrying structures," *IEEE Sensors Lett.*, vol. 3, no. 6, pp. 1–4, Jun. 2019.
- [13] Z. Xing, J. Li, and D. Viehland, "Giant magnetoelectric effect in Pb(Zr,Ti)O₃-bimorph/NdFeB laminate device," *Appl. Phys. Lett.*, vol. 93, no. 1, Jul. 2008, Art. no. 013505.
- [14] J. Ryu, J.-E. Kang, Y. Zhou, S.-Y. Choi, W.-H. Yoon, D.-S. Park, J.-J. Choi, B.-D. Hahn, C.-W. Ahn, J.-W. Kim, Y.-D. Kim, S. Priya, S. Y. Lee, S. Jeong, and D.-Y. Jeong, "Ubiquitous magneto-mechano-electric generator," *Energy Environ. Sci.*, vol. 8, no. 8, pp. 2402–2408, 2015.
- [15] N. M. Roscoe and M. D. Judd, "Harvesting energy from magnetic fields to power condition monitoring sensors," *IEEE Sensors J.*, vol. 13, no. 6, pp. 2263–2270, Jun. 2013.
- [16] L. Du, C. Wang, X. Li, L. Yang, Y. Mi, and C. Sun, "A novel power supply of online monitoring systems for power transmission lines," *IEEE Trans. Ind. Electron.*, vol. 57, no. 8, pp. 2889–2895, Aug. 2010.
- [17] S. Paul and J. Chang, "Design of novel electromagnetic energy harvester to power a deicing robot and monitoring sensors for transmission lines," *Energy Convers. Manage.*, vol. 197, Oct. 2019, Art. no. 111868.
- [18] P. Maharjan, M. Salauddin, H. Cho, and J. Y. Park, "An indoor power line based magnetic field energy harvester for self-powered wireless sensors in smart home applications," *Appl. Energy*, vol. 232, pp. 398–408, Dec. 2018.
- [19] R. White, D.-S. Nguyen, Z. Wu, and P. Wright, "Atmospheric sensors and energy harvesters on overhead power lines," *Sensors*, vol. 18, no. 2, p. 114, Jan. 2018.
- [20] J. Moon and S. B. Leeb, "Analysis model for magnetic energy harvesters," *IEEE Trans. Power Electron.*, vol. 30, no. 8, pp. 4302–4311, Aug. 2015.
- [21] S. Yuan, Y. Huang, J. Zhou, Q. Xu, C. Song, and P. Thompson, "Magnetic field energy harvesting under overhead power lines," *IEEE Trans. Power Electron.*, vol. 30, no. 11, pp. 6191–6202, Nov. 2015.
- [22] F. Yang, L. Du, W. Chen, J. Li, Y. Wang, and D. Wang, "Hybrid energy harvesting for condition monitoring sensors in power grids," *Energy*, vol. 118, pp. 435–445, Jan. 2017.
- [23] R. Moghe, F. C. Lambert, and D. Divan, "Smart 'stick-on' sensors for the smart grid," *IEEE Trans. Smart Grid*, vol. 3, no. 1, pp. 241–252, Oct. 2011.
- [24] S. Yuan, Y. Huang, J. Zhou, Q. Xu, C. Song, and G. Yuan, "A high-efficiency helical core for magnetic field energy harvesting," *IEEE Trans. Power Electron.*, vol. 32, no. 7, pp. 5365–5376, Jul. 2017.
- [25] Y. Zhuang, C. Xu, C. Song, A. Chen, W. L. Y. Huang, and J. Zhou, "Improving current transformer-based energy extraction from AC power lines by manipulating magnetic field," *IEEE Trans. Ind. Electron.*, vol. 67, no. 11, pp. 9471–9479, Nov. 2020.
- [26] J. García-Martín, J. Gómez-Gil, and E. Vázquez-Sánchez, "Non-destructive techniques based on eddy current testing," *Sensors*, vol. 11, no. 3, pp. 2525–2565, Feb. 2011.
- [27] D. Jiles, *Introduction to Magnetism and Magnetic Materials*. Boca Raton, FL, USA: CRC Press, 2015.
- [28] R. J. Hill, "Electric railway traction. Part 3: Traction power supplies," *Power Eng. J.*, vol. 8, no. 6, pp. 275–286, Dec. 1994.
- [29] F. Nyberg and R. Pollard, *Network Rail A Guide to Overhead Electrification*. Accessed: Mar. 9, 2021. [Online]. Available: https://www.bathnes.gov.uk/sites/default/files/sitedocuments/Planning-and-Building-Control/Planning/nr_a_guide_to_overhead_electrification.pdf
- [30] Y. Xu, S. Bader, and B. Oelmann, "Design, modeling and optimization of an m-shaped variable reluctance energy harvester for rotating applications," *Energy Convers. Manage.*, vol. 195, pp. 1280–1294, Sep. 2019.
- [31] Y. Singh, *Electro Magnetic Field Theory*. London, U.K.: Pearson, 2011.
- [32] C. Inc. *COMSOL Documentation*. [Online]. Available: https://doc.comsol.com/5.5/docserver#!/com.comsol.help.acdc/acdc Ug_magnetic_fields_08.087.html
- [33] (Mar. 9, 2021), *Multilayer Ceramic Capacitors/Axial and Radial Leaded*. Accessed: Mar. 9, 2021. [Online]. Available: <https://sh.kemet.com/Lists/FileStore/Ceramic%20Molded%20Axial-Radial%20X7R.pdf>
- [34] E. Kaverine, S. Palud, F. Colombel, and M. Himdi, "Investigation on an effective magnetic permeability of the rod-shaped ferrites," *Prog. Electro-magn. Res. Lett.*, vol. 65, pp. 43–48, 2017.



YANG KUANG received the B.Eng. and M.Eng. degrees in mechanical engineering from Central South University, China, and the Ph.D. degree in high power piezoelectric transducers from the University of Dundee, in 2014. Since 2014, he has been working with the University of Exeter, as an Associate Research Fellow and later as a Research Fellow. His main research interest includes self-power wireless sensing systems enabled by energy harvesting.



devices using novel and low-power techniques.

ZHENG JUN CHEW (Member, IEEE) received the B.Eng. degree in electronic and electrical engineering from the University of Strathclyde, Glasgow, U.K., in 2010, and the Ph.D. degree in electronic and electrical engineering from Swansea University, Swansea, U.K., in 2014. He is currently a Research Fellow with the Energy Harvesting Research Group, University of Exeter, Exeter, U.K. His current research interest includes power management module for energy harvesting



MEILING ZHU received the B.Eng., M.Eng., and Ph.D. degrees from Southeast University, Nanjing, China, in 1989, 1992, and 1995, respectively. She is currently a Professor and the Chair of mechanical engineering and the Head of the Energy Harvesting Research Group with the University of Exeter, U.K. Her current research interests include piezoelectric energy harvesting powered wireless communication and sensor nodes.

...



Research Group, University of Exeter. His current research interest includes energy harvesting powered wireless sensing systems for the Industrial Internet of Things.

TINGWEN RUAN received the B.Eng. degree from the Nanjing University of Posts and Telecommunications, Nanjing, China, in 2012, and the Ph.D. degree in energy-aware approaches for energy harvesting powered wireless sensor systems from the University of Exeter, U.K., in 2019. In 2013, he was a Technical Support Engineer with Zhongxing Telecommunication Equipment Corporation, China. He is currently working as a Research Associate with the Energy Harvesting